Frustrated Packing in Simple Structures: Chemical Pressure Hindrance to Isolobal Bonds in the $TiAl_3$ type and $ZrAl_{2.6}Sn_{0.4}$

Kendall R. Kamp and Daniel C. Fredrickson*

Department of Chemistry, University of Wisconsin-Madison, 1101 University Avenue, Madison, WI, 53706, United States

ABSTRACT: While simple close-packed arrangements convey a sense of optimization, they can in fact host competition between different types of interactions. The $TiAl_3$ structure type, for example, represents one of a series of ordered TE_3 variants (T = transition metal, E = main group element) of the face-centered cubic structure, alongside the $AuCu_3$ and $ZrAl_3$ types. These structures differ in their T-T connectivity corresponding to the 18−*n* rule: electronic pseudogaps occur at electron concentrations of 18−*n*/T atom, where *n* is the number of electron pairs each T atom shares with other T atoms in T-T isolobal bonds. Facile stacking variations interrelate these structures, presumably setting the stage for an electronically precise series. However, the prototype of the $TiAl_3$ type itself violates the 18−*n* rule, with its count of 13 electrons/Ti atom calling for *n* = 5 rather than the 4 isolobal T-T bonds/T atom available in this type. Here, we investigate the factors underlying this deviation from the 18−*n* rule, and their relation to the new $TiAl_3$-type compound $ZrAl_{3-x}Sn_x$ ($x \sim 0.4$). First, the relative stabilities of the $TiAl_3$ and $ZrAl_3$ types are compared for TAl_3 compounds (T = Zr and Ti). While for T = Zr the structure adhering to the 18−*n* rule is highly preferred, for T = Ti the energy difference essentially vanishes. This trend is connected through DFT-Chemical Pressure (CP) analysis to a tension that emerges in $TiAl_3$ between the optimization of the T-T isolobal bonds and the space requirements of Al-Al contacts elsewhere. This picture elucidates the transition of $ZrAl_3$ from its own type to the $TiAl_3$-type upon partial Sn substitution in $ZrAl_{2.6}Sn_{0.4}$: the incorporation of Sn brings the electron count closer to that predicted for the $TiAl_3$ type, while electronegativity and CP direct the larger Sn atoms to the site that resists isolobal bond formation in $TiAl_3$.

1. INTRODUCTION

It is sometimes the exceptions to a rule that teach us the most about chemistry. Violations to the octet rule of main group molecules, the limitations on rotational symmetries in periodic structures, and the 18-electron rule of coordination compounds point to the wider realms of hypo- and hyper-valent bonding,[1-3] quasicrystalline order,[4-6] and transition metal reactivity and catalysis,[7-9] respectively. In terms of the last of these, a broader potential for the 18-electron rule is apparent in its extension to the structural chemistry of intermetallic phases. This extension takes the form of the 18−*n* rule for T-E compounds (T=transition metal, E = main group element): for a T atom to achieve a closed shell electron configuration it requires 18−*n* electrons, in which *n* is the number of T-T contacts supported by surrounding E atoms to create a multicenter function isolobal to a classical bond.[10] While this bonding scheme has been applied to over 46 intermetallic structure types (representing hundreds of compounds), it remains unclear under what conditions it will be broken and what lessons about structural chemistry such exceptions have to offer.[10]

A prominent exception to the 18−*n* rule is $TiAl_3$, the prototype for a structure type that is adopted by 19 binary compounds.[11,12] This compound belongs to a broader TE_3 series consisting of three closely related structure types: $AuCu_3$ (as adopted by $ScAl_3$), $ZrAl_3$ and $TiAl_3$.[13-19] Each of these structures is based on ordered variants of the FCC structure.[20,21] In the $AuCu_3$-type $ScAl_3$, T atoms form a primitive cubic arrangement (through sharing square faces of their Al_{12} cuboctahedral coordination environments) giving each T atom an octahedral arrangement of six T atom neighbors (Figure 1, left). In the $ZrAl_3$ type, this network is broken up by shifts in the stacking into layers of T cubes, reducing the number of T neighbors to five: four in the *ab* plane making square nets plus a fifth along *c* (Figure 1, middle). This breakdown of the T-T connectivity continues in the $TiAl_3$ type where the T atoms now form square nets of T atoms (Figure 1, right), such that each has four T neighbors. Overall, these differing arrangements provide each structure with a different number of T-T contacts: six for $AuCu_3$, five for $ZrAl_3$ and four for $TiAl_3$, which according to the 18−*n* rule should prefer different electron counts.[22]

Previously, this electron deficiency in $TiAl_3$ was rationalized in terms of the compensatory effect of Ti-Ti π interactions, but this picture alone does not explain why $TiAl_3$ deviates from the 18−*n* rule while the isoelectronic $ZrAl_3$ and $HfAl_3$ compounds adhere to it.[10] In this Article, we will investigate the factors that hinder the Ti atoms of $TiAl_3$ from optimizing its bonding scheme with a fifth isolobal bond. We start by comparing the energetics of the $TiAl_3$ (n = 4) and $ZrAl_3$ (n = 5) structure types for T = Ti and Zr, discovering that the advantages to following the 18−*n* rule are significantly lower in the former case. This will be traced to Chemical Pressure (CP)[23-26] issues in the formation of isolobal bonds, where the fifth isolobal bond demands compression of overly short Al-Al contacts elsewhere in the structure. With this theoretical picture in hand, we will then present the synthesis and crystal structure of a new $TiAl_3$-type compound, $ZrAl_{3-x}Sn_x$ ($x \sim 0.4$), with the site-preferences and higher electron count of the Sn atoms serve to destabilize the n = 5 structure of the unsubstituted compound $ZrAl_3$. In this way, $TiAl_3$'s violation of the 18−*n* rule points the way to a broader scheme for how isolobal

bonds interact with atomic packing constraints in intermetallic structures.

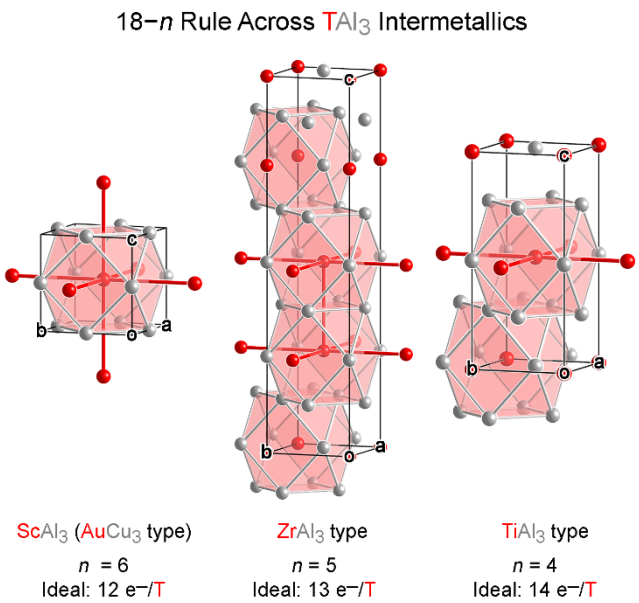

Figure 1. Series of TAl_3 (T = transition metal element) structures based on different stacking arrangements of the FCC structure. In each structure the number of T-T contacts dictates an ideal electron count predicted by the 18−*n* rule.

2. EXPERIMENTAL SECTION

2.1. Electronic structure analysis. Structure optimization and the calculation of total energies, band energies and density of states (DOS) distributions were performed for TAl_3 structures (T = Ti and Zr) in the $ZrAl_3$ and $TiAl_3$ types using the Vienna ab initio Simulation Package (VASP).[27-30] The calculations employed the projector augmented wave (PAW)[31,32] potentials provided with the program and the generalized gradient approximation (GGA)[31-33] and were carried out in the high precision mode (corresponding to an energy cutoff of 240.437 eV). 16 × 16 × 4 and 16 × 16 × 8 Γ centered k-point meshes were used for $ZrAl_3$-type and $TiAl_3$-type structures, respectively.[34] Gaussian broadening was applied to the DOS distributions to make their general features more apparent. In addition, atomic charges were obtained from the electron densities using the Quantum Theory of Atoms in Molecules (QTAIM) approach using the Bader program.[35-38]

Energetic contributions to the various interactions in the isolobal bonding functions were also analyzed using the reversed approximation Molecular Orbital (raMO) method.[39,40] For this analysis, best fit Hückel parameters were refined against the DFT results using the eHtuner program[41] and the resulting parameters were used to calculate the simple Hückel Γ point Hamiltonian matrix for a 3 × 3 × 2 supercell. This matrix was then loaded into the in-house MATLAB program raMOmovie for the raMO reconstructions. Additional computational details, including a table of the DFT-calibrated Hückel parameters are provided in the Supporting Information.

2.2. DFT-Chemical Pressure (CP) Analysis. DFT-CP schemes were generated for $AuCu_3$-, $ZrAl_3$- and $TiAl_3$-type versions of both $ZrAl_3$ and $TiAl_3$ as well as 3 ordered models of $TiAl_3$-type $ZrAl_2Sn$. First, the geometries of the phases were optimized with the ABINIT[42-45] program using LDA-DFT and Hartwigsen-Goedecker-Hutter (HGH)[46] norm-conserving pseudopotentials. The energy cutoff was set to 40 Ha, while the k-point meshes are provided in the Supporting Information. Single-point calculations were then carried out at the cell's equilibrium geometry as well as slightly expanded and contracted volumes to generate the kinetic energy densities, electron densities, and wavefunctions at each volume, as well as the local components of the Kohn-Sham potential. The wavefunctions used to resolve the nonlocal pseudopotential energy into atomic contributions using the in-house program nonlocal_15o3.[26] The output of these calculations was then used as input in the DFT-CPpackage2 program, with which the CP maps were generated using the core-unwarping process and the separation of the E_{Ewald} and E_α terms into localized and itinerant components.[26] The pressure maps were divided into contact volumes based on the Hirschfeld-inspired scheme, within which interatomic pressures were obtained by averaging and projected onto atom-centered spherical harmonics ($l \leq 6$). The resulting schemes were visualized with an in-house MATLAB program.

For the determination of the contact volumes, free-ion electron densities were generated with the Atomic Pseudopotentials Engine (APE)[47], with charges set to fractions of those obtained in the Bader analysis (on the GGA-DFT electronic structures from VASP; see above). CP schemes were plotted with differing ionicities as a percentage of the total Bader charge. In the main text, we show results for neutral (0%) ionicity, while additional schemes are given in the Supporting Information. The ionicity dependence was found to be significantly reduced by mapping the atomic nonlocal energies in proportion to the valence electron density surrounding the respective atomic centers (rather than using length-scales involving the non-local projector operators), and this approach was adopted for this work.

The determination of itinerant and localized electrons for the partitioning of the E_{Ewald} and E_α terms was determined for each structure through a calibration of CPs at highly expanded and contracted volumes (centered at linear scales of 120 % and 80 % of the equilibrium geometry, respectively). At both the highly expanded and contracted geometries, the number of localized electrons on each atom was tuned so that the pressures on each atom were approximately equal in magnitude (while keeping the number for the site with the most negative initial pressure equal to 0). The number of localized and itinerant electrons used in the equilibrium volume schemes was the average of those obtained for each site for the expanded and contracted structures.

2.3. Synthesis. Samples of $ZrAl_{3-x}Sn_x$ were prepared by grinding together mixtures of the elements (Zr powder, Strem, 99.5%; Al powders, Strem, 99.7%; and Sn powders, Alfa Aesar, 99.8%) with Sn-rich Zr:Al:Sn compositions of 1:2.5:2 and 1:3:2, and total sample masses of about 0.5 g. The samples were poured into alumina crucibles, each of which was placed in a fused silica tube and capped with another alumina crucible. The tubes were then sealed under vacuum and heated in a muffle furnace to 900°C in 12 h, held there for 24 h, and then quickly cooled to 600°C, where they were annealed for 2 weeks. The samples were then either quenched into ice water or cooled to room temperature at a rate of 20°C/h. All synthesis yielded dark gray block-shaped crystals suitable for single crystal X-ray diffraction analysis.

2.4. Powder X-ray Diffraction Analysis. Portions of each sample were ground to a powder with an agate mortar and pestle, then mounted on a zero-diffraction Si background plate. Powder diffraction data were measured with a Bruker D8 Advance Powder X-ray Diffractometer with Cu Kα radiation (λ = 1.5418 Å), over a 2θ range of 10-90° with a 0.02° increment size and a 0.9s exposure time. The resulting patterns were analyzed with the Match! Software.[48]

2.5. Single Crystal X-ray Diffraction Analysis. Dark gray colored block-shaped crystals were picked from the samples and mounted on glass fibers with epoxy. The crystals were analyzed on an Oxford Diffraction Xcalibur E Diffractometer equipped with a Mo Kα (λ = 0.71073 Å) sealed-tube X-ray source at room temperature or a Bruker Quazar APEX2 diffractometer also equipped with a Mo Kα IμS source. The CrysalisPro[49] software and APEX3[50-52] software were used for the generation of the run lists and processing frame data. Data sets of the crystals were indexed with tetragonal unit cells with $a \approx 3.97 - 4.00$ Å and $c \approx 9.08 - 9.12$ Å. Analysis of systematic absences suggested the space group *I*4/*mmm*. Three symmetrically distinct atomic positions were assigned using a charge flipping algorithm as implemented by the SUPERFLIP program.[53,54] The resulting solution was refined

on F^2 in JANA2006.[55,56] One symmetry distinct atomic site exhibited compositional disorder and was modeled as Al/Sn mixed site with a total occupancy of 1.0.

2.6. Elemental Analysis with Energy Dispersive X-ray Spectroscopy (EDS). Fragments of the samples were cured in epoxy and polished with diamond lapping films at decreasing grit (9-0.5 μm) to achieve a smooth flat surface. The samples were then carbon coated (20 nm) and analyzed in a Hitachi S-3100N scanning electron microscope (voltage = 30 keV) equipped with an Oxford Instrument X-Act EDS detector and analyzed using the Oxford Instruments Aztec software package (version 3.2). Imaging in the backscattered electron mode showed two distinct compounds embedded in a Sn matrix, one appearing dark gray ($ZrSn_2$) and the other lighter gray whose composition was measured as $ZrAl_{2.73(5)}Sn_{0.43(3)}$ (from an average over 13 points).

2.7. Phonon Band Calculations. To validate the CP schemes, phonon band structures of $TiAl_3$-type $ZrAl_3$ with both semicore and valence only HGH pseudopotentials,[46] as well as $TiAl_3$ in both the $TiAl_3$ and $ZrAl_3$ structure types, were calculated using the linear response method in ABINIT.[43-45] The optimized geometry was used to produce a q-point for each k-point in the Γ-centered mesh. Non-self-consistent calculations were then done at each q-point to produce linear-response functions. From these results, the ABINIT utilities mrgddb and anaddb were used to determine force constants.[42] The resulting phonon modes were visualized with the inhouse MATLAB program Figuretool2 and are presented in the Supporting Information.

3. RESULTS AND DISCUSSION

3.1. Relative Stabilities of the $TiAl_3$ and $ZrAl_3$ Structure Types. Our investigations into the $TiAl_3$ and $ZrAl_3$ structures are rooted in the question of why two compounds based on isoelectronic metals crystallize in different structure types. The interconversion between the $TiAl_3$ and $ZrAl_3$ types can be thought of as shifts in the stacking of layers of $T@Al_{12}$ cuboctahedra, resulting in different ordered variants of the FCC structure. As the primary difference that emerges from these structures is the T-T connectivity, it seems surprising that one compound would prefer a structure with the Fermi energy in a pseudogap (following the 18–*n* rule), while the other would take an alternative arrangement. In this section, we will begin exploring the driving forces here with comparisons of the energetics of TAl_3 (T = Ti and Zr) structures in these two types.

The energies of formation calculated with GGA-DFT for TAl_3 (T = Ti and Zr) in the $TiAl_3$ and $ZrAl_3$ types are plotted in Figure 2. Here, the formation energy of the experimentally observed structure type for each compound is plotted as a solid horizontal line, while that for the hypothetical alternative is indicated with a dotted line. Overall, the formation energies are all negative in the range of -2.0 and -1.5 eV/FU. They are more negative for the Zr-containing phases, regardless of structure type, suggesting a higher impetus for compound formation in the Zr-Al system than in the Ti-Al one.

Let's begin by examining the energetic trends for the T = Zr case. The $ZrAl_3$-type structure is lower in energy, consistent with experimental observations. The hypothetical $TiAl_3$-type structure lies ~0.1 eV/FU higher in energy. These results align with the expectations of the 18–*n* rule, in which the *n* = 5 $ZrAl_3$ type matches the 13 electron/Zr atom count of the compound. The $TiAl_3$ type is missing one T-T contact for each T atom, and the ~0.2 eV cost per T_2 pair to adopt this structure could be interpreted as an effective strength of the T-T isolobal bond.

The case for T = Ti, the same order is observed in terms of the energies, but the energy difference is now much smaller, being only about ~0.03 eV/FU. The stabilizing effect of adhering to the 18–*n* rule here thus appears greatly reduced. In fact the structure with the slightly higher energy (at T = 0 K, where entropic effects do not come into play) is the one generally associated with this compound, aligns with the observation that $TiAl_3$ slowly transforms to a $ZrAl_3$-type variant at (relatively) low temperatures.[57] The weakened potential for T-T isolobal bonding in $TiAl_3$ led us to investigate how the electronic and atomic packing situations change between $ZrAl_3$ and $TiAl_3$ to create this effect.

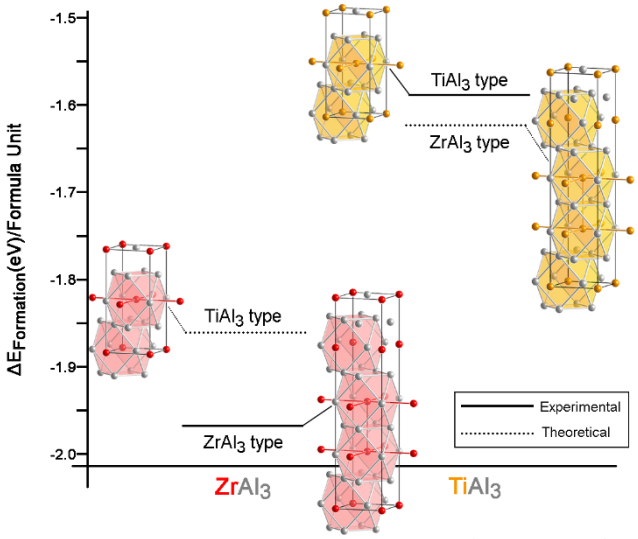

Figure 2. GGA-DFT energies of formation of TAl_3 (T = Zr and Ti) in the $ZrAl_3$ and $TiAl_3$ structure types. The formation energies for experimentally observed compounds are shown with solid lines, while those for hypothetical structures are given with dotted lines. Note that the structure predicted by the 18–*n* rule, the $ZrAl_3$ type, is preferred in both cases, but the energy difference is smaller for T = Ti.

3.2. Electron Counting in the $ZrAl_3$ and $TiAl_3$ Structure Types. The electronic density of states (DOS) distributions of the TAl_3 compounds provide a window into how switching Zr with Ti influences the bonding scheme. Let's begin with $ZrAl_3$ in its own type (Figure 3, far left). Here, the Fermi energy (E_F) lies in a pseudogap suggesting that the compound has a well-optimized electron count, much as a large HOMO-LUMO gap is correlated with stability in molecules. This reflects the structure's adherence to the 18–*n* rule. Here, each Zr has five proximal Zr neighbors (*n* = 5), such that 18 − 5 = 13 electrons needed per Zr atom, which matches the count given by $ZrAl_3$'s stoichiometry (4 + 3 × 3 = 13). Moving to $ZrAl_3$ in the $TiAl_3$ type (where *n* = 4 rather than 5) leads to a much less picturesque DOS distribution. The E_F now falls below the local minimum of the curve (Figure 3, middle left), reflecting that the electron count of 13 per Zr atom is deficient relative to the 18–*n* count of 14 for this type. These results affirm the electronic driving force for $ZrAl_3$ to adopt the structure that follows the 18–*n* rule.

As Ti and Zr are isoelectronic, one could expect analogous trends for $TiAl_3$ in these structure types. Indeed, $TiAl_3$ in the $ZrAl_3$ structure type exhibits a clear DOS minimum at the E_F, in-line with it being an electron precise 18–*n* compound. Likewise, $TiAl_3$ in its own type appears to be electron deficient with its E_F falling below the pseudogap in the DOS curve. This is consistent with the $TiAl_3$ being one electron per Ti atom short of the 18 − 4 = 14 count needed for a complete 18 electron configurations in this structure.

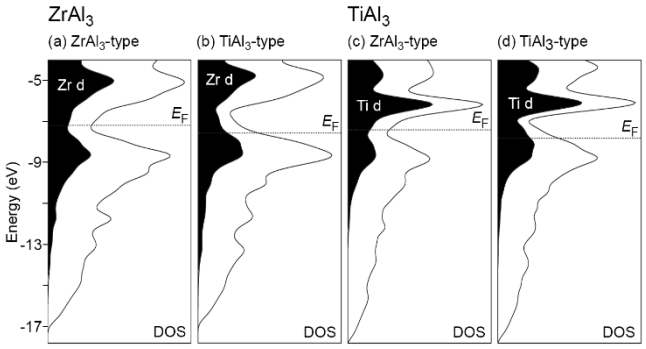

Figure 3. GGA-DFT DOS distributions for TAl_3 compounds (T = Zr and Ti) in the $ZrAl_3$ and $TiAl_3$ structure types. In each curve, there is a clear pseudogap between -8 and -6 eV, corresponding approximately to their 18–*n* electron counts. Contributions of Zr and Ti d character are shaded in black.

3.3. The Nature of the Isolobal Bond. Overall, then, the DOS distributions of the TAl_3 compounds in these structures follow the expectations of the 18–*n* rule. Little indication is given for why the energetic cost for forming $TiAl_3$ type (*n* = 4, electron poor) rather than the $ZrAl_3$ type (*n* = 5, electron balanced) would be 3 times lower for T = Ti than T = Zr. As one of the most obvious differences between Ti and Zr is their atomic sizes (r_{Zr} = 1.6 Å and r_{Ti} = 1.47 Å),[58] a possibility is that the differing degrees of T-T bonding overlap in the two cases could play a role. To investigate this possibility, we now examine the isolobal bonding functions for these structures in more detail. We first derive isolobal bonding functions for TAl_3 compounds (T = Ti and Zr) in the $ZrAl_3$ and $TiAl_3$ types using the reverse approximation Molecular Orbital (raMO) analysis.[40]

Here, the occupied crystal orbitals of DFT-calibrated Hückel models of the structures are used as basis sets from the reconstruction of a multi-center function of s-like symmetry centered on T-T contacts within the structures. The resulting functions are shown in Figure 4, where for each case a T_2Al_4 octahedron is decorated with 6 in-phase hybrid orbitals pointing to the center of the polyhedron. As they are constructed from similarity transforms on the occupied crystal orbitals, each of these represent an electron pair that exists in the full electronic structure.

Once we have these functions, we can decompose their energies into Hamilton populations (HPs) corresponding to the onsite and pairwise contributions to the energy. Below each of the raMO functions in Figure 4, we compare the HPs for the T-T and T-Al interactions. One feature of note here is the relatively small magnitude of the direct T-T interactions, which are in most cases less than 0.1 eV. The stabilization provided by in-phase combination of T lobes appears instead to emerge overwhelmingly from their shared overlap with the bridging Al atoms. Such is, of course, understandable from rather large T-T distances that are often seen in isolobal bonds, e.g. 3.82 Å and 3.87 Å in the LDA-optimized structure of the T = Ti $ZrAl_3$-type phase.

Another trend is that the values for the T = Zr raMOs are uniformly more negative than the corresponding ones in the T = Ti functions, consistent with the Zr atoms' larger size and more diffuse d orbitals. In this way, the isolobal bonding functions in the T = Zr phases are indeed more stabilizing than in their T = Ti analogues. This difference on its own, however, hardly explains why the breaking the fifth isolobal bond per T atom in the $ZrAl_3$ type to form the $TiAl_3$ type should be essentially energy neutral for T = Ti. In the next section, we will examine the role another factor, the size requirements of the atoms, plays in these trends.

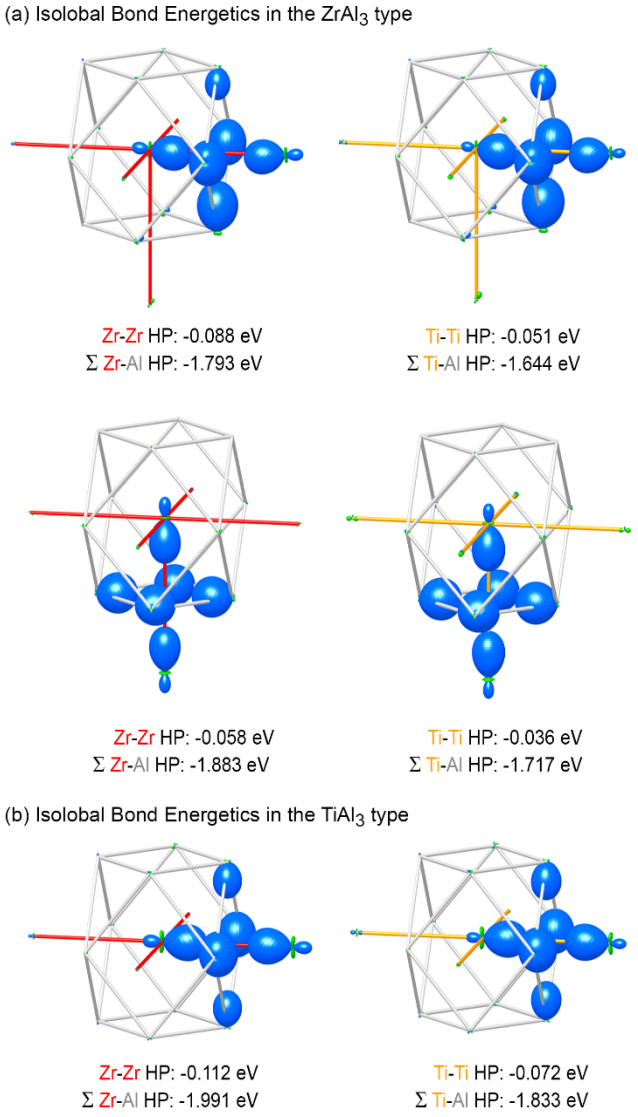

Figure 4. Energetics of isolobal bonds in (a) $ZrAl_3$-type $TiAl_3$ and $ZrAl_3$ and (b) $TiAl_3$-type $TiAl_3$ and $ZrAl_3$. Hamilton populations (HP) for the Zr-Zr and Zr-Al interactions are generally more negative than their Ti-Ti and Ti-Al counterparts.

3.4. Atomic Packing Strains in $ZrAl_3$ and $TiAl_3$. The packing constraints and their potential role in impeding isolobal bond formation in TAl_3 compounds can be visualized with DFT-Chemical Pressure (CP) analysis. In this method, the macroscopic internal pressure of a compound is resolved into a 3D pressure map that is interpreted in terms of interatomic interactions, with positive and negative interatomic chemical pressures (CPs) corresponding to local driving forces for the expansion or contraction of the structure. With this approach, we can examine how the degree of optimization of the T-T, T-Al, and Al-Al distances changes across the TAl_3 series of FCC-derived structure types with different *n* values: $AuCu_3$ (*n* = 6), $ZrAl_3$ (*n* = 5), and $TiAl_3$ (*n* = 4).

In Figure 5, we compare CP schemes calculated for the T = Ti versions of each of these structure types. Here, the pressures are plotted radially around each atomic center, with the size of the lobe being proportional to the magnitude of the sum of the pressure contributions along that direction. The color of each lobe signifies the sign of the pressure: white for positive pressure (exhibited by overly short contacts desiring expansion), black for negative pressure (displayed by overly long contacts desiring contraction).

Beginning with the $AuCu_3$-type T = Ti structure (Figure 5a), the central Ti cation experiences isotropic positive pressures towards each of its 12 Al neighbors, signifying that Ti is too large for this coordination environment and would benefit from the structure's expansion. This is impeded, however, by the negative CPs along the Al-Al contacts. Note that the effective Ti-Ti attraction expected from the presence of isolobal bonding does not appear to be urging shorter contacts here, with Ti-Ti contacts instead representing a compromise between overly-short Ti-Al distances and overly-long Al-Al ones.

One might wonder how much the electron-rich nature of the structure (13 electrons/Ti from the stoichiometry compared to the 12 electrons/Ti idealized by the 18−*n* rule) influences this balance of interactions. The CP schemes for the $ZrAl_3$- and $TiAl_3$-type structures show qualitatively similar features. As these are electron precise and electron poor structures, respectively, these similarities suggest that the atomic packing factor are largely separable from placement of the E_F relative to the pseudogaps (at least for this range of deviations from the 18−*n* rule).

Let's now focus more closely on the CP scheme of the $ZrAl_3$-type T = Ti structure (Figure 5b). As we were just hinting, it shows many of the same features as the $AuCu_3$-type structure: positive heteroatomic Ti-Al pressures against a backdrop of predominantly negative Al-Al pressures. There are important differences, however, in the local details. The positive CP surfaces surrounding the Ti atoms are now much less isotropic, as they are missing lobes toward the Al atoms on the side above or below where no Ti-Ti contact is present. The absence of one isolobal bonding contact has led to more optimal Ti-Al contacts. This asymmetry of the Ti coordination environment and CP scheme allows the Ti atoms to move off of the center of their cuboctahedral environments toward the remaining Ti neighbor along the *c*-axis, which could serve to strengthen the isolobal bonds at these contacts.

Differences can also be perceived in the CPs of the Al sublattice. The majority of the Al-Al contacts experience negative CP, with the most intense being between layers along the *c*-direction where the $AuCu_3$-type stacking is maintained. However, the Al atoms at the stacking shift exhibit significantly smaller negative CPs. In fact, the contacts between the Al atoms within this *ab*-plane suffer from positive CP, with net interatomic pressures of +31.7 GPa. At this point in the structure, the Al atoms are actually bumping into each other rather than struggling to get closer.

The presence of positive Al-Al CP here represents a remarkable change in the balance of forces from the $AuCu_3$-type T = Ti compound. In the $AuCu_3$ type, the positive pressures were entirely within the Ti-Al interactions that bridge the isolobal Ti-Ti bonds, which were balanced by Al-Al negative pressures that encircle those same bonds. In other words, both the forces calling expanding and contraction of the structure are directly involved in defining the shape of the $TiAl_4Ti$ octahedra that make up the isolobal bond. In the $ZrAl_3$-type, the Al-Al positive CPs at the stacking shift are not involved in bridging any Ti-Ti interactions. Instead, they represent external resistance to the structural preferences of the isolobal bonds.

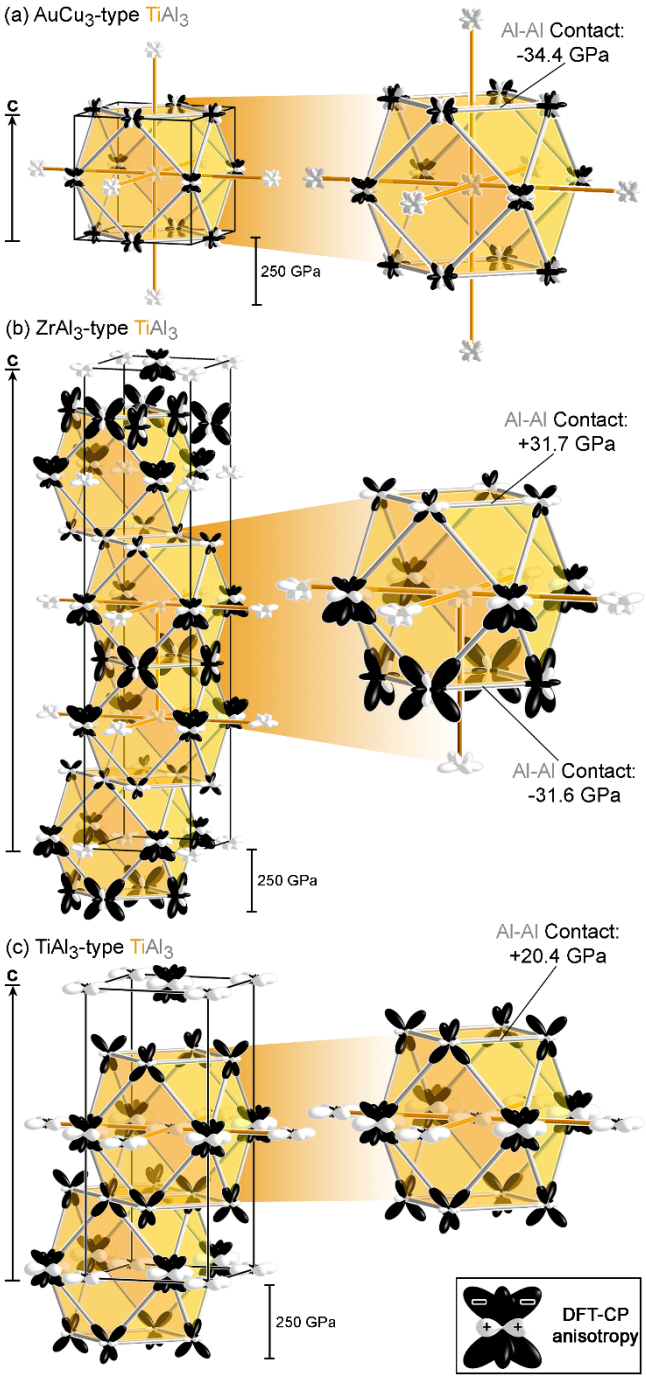

Figure 5. CP schemes for $TiAl_3$ in each of the TAl_3 structure types with emphasis on the repeating T@Al_{12} cuboctahedral unit. (a) $AuCu_3$-type $TiAl_3$, (b) $ZrAl_3$-type $TiAl_3$ and (c) $TiAl_3$-type $TiAl_3$.

Such competition can be seen by comparing the CP features of the Al atoms in these square nets with those on the square nets that provide bridging interactions to the Ti-Ti contacts oriented along *c*. The Al-Al distances in both square nets are constrained by periodicity of the structure to be equal, at $a/\sqrt{2}$. However, the Al atoms involved in the isolobal bonds experience negative rather than positive CP (-31.6 GPa), pushing the volume of the structure in the opposite

direction. This unequal involvement is isolobal bonding leads to different preferences for the unit cell *a* parameter.

Breaking the remaining isolobal bond along *c*, as in the $TiAl_3$ type, offers a path to resolving this issue. Here, the Ti-Ti isolobal bonds are now restricted to square nets in individual *ab*-planes, with the in-plane Ti-Al contacts experiencing positive CP analogous to that in the other structures, and in fact small negative pressures have appeared between the Ti atoms and the Al atoms above and below them along *c*. The Al atoms in these adjacent layers both represent stacking shifts relative to the original $AuCu_3$ type. As they are now symmetrically equivalent, the layers no longer have cause to compete with each other. Instead, both exhibit smaller in-plane Al-Al positive CPs (+20.4 GPa), consistent with the preference for longer distances of the Al-Al contacts less involved in isolobal bonds. Overall, then, the CP analysis of the T = Ti series of structures indicates that the formation 18−*n* structure, the $ZrAl_3$-type, comes with a cost. The Al-Al contraction around the remaining Ti-Ti isolobal bonds along *c* is resisted by positive pressures in the Al atom layers left out of these interactions. Moving to the $TiAl_3$ type soothes this tension, with lower Al-Al positive CPs appearing in the stacking shift layers, even while the resulting structure is one electron/Ti atom poor.

How do these trends change as we go to T = Zr, where the $ZrAl_3$ type is the observed structure? At first glance, the CP schemes for T = Zr structures (Figure 6) exhibit qualitatively similar features to those of their T = Ti analogues. The Zr cation experiences positive pressure from the Al neighbors bridging Zr-Zr isolobal bonds, with most of the Al-Al contacts showing negative CP.

There are key differences, however, in the CPs of the shift layers of the $ZrAl_3$- and $TiAl_3$-type structures. Whereas in the T = Ti layers positive CPs appeared between the Al atoms in the shift layers, in the T = Zr case, these are now negative. Al-Al repulsion is no longer serving as a counter force resisting the contraction for the formation of isolobal bonds. In fact, moving from the $ZrAl_3$ type to the $TiAl_3$ type intensifies the negative pressure within the stacking shift layers. As such, $ZrAl_3$ does not experience the same barriers as $TiAl_3$ to the formation of the full five isolobal bonds needed to achieve 18 electron configurations on the T atoms.

This difference can be attributed to the sizes of the T atoms. As the Ti atoms are smaller than Zr ones, the ideal T-Al distances in the Ti-Ti isolobal bonds will naturally be shorter than in their Zr-Zr analogues. $TiAl_3$ is thus more subject to crowding of the Al atoms away from the key T-Al interactions than $ZrAl_3$ is. From this picture, the scope of the 18−*n* rule becomes a little clearer: while 18−*n* electrons will be required for each T atom to achieve a filled octadecet, the atomic packing factor can play a role in how many isolobal bonds can be formed. In the next section, we will explore how these factors underlie the transformation of the $ZrAl_3$-type T = Zr phase to the $TiAl_3$ type when Al is partially substituted with Sn.

3.5. Stabilization of the $TiAl_3$ type in $ZrAl_{3-x}Sn_x$. So far, we have focused on the factors leading to $TiAl_3$ crystallizing in a structure that breaks the 18−*n* rule, uncovering how repulsion between Al atoms inhibits the formation of a fifth isolobal bond on each Ti atom. With this picture in hand, we can readily interpret a new experimental observation we have made in the Zr-Al-Sn system. This system represents an intriguing realm for synthetic exploration as no ternary phase diagram is available and no ternary structures are reported in the Inorganic Crystal Structure Database (ICSD). [11,59]

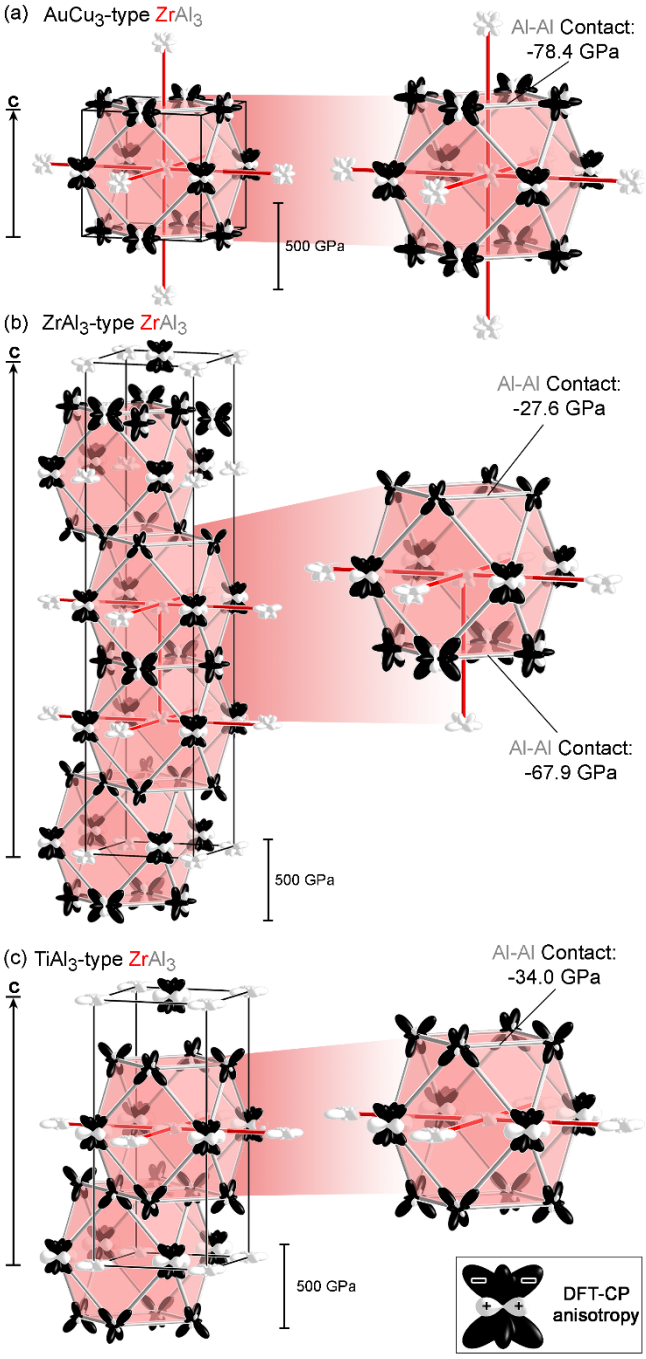

Figure 6. CP schemes of $ZrAl_3$ in each of the TAl_3 structure types. (a) $AuCu_3$-type $ZrAl_3$, (b) $ZrAl_3$ in its own structure type, and (c) $TiAl_3$-type $ZrAl_3$.

In our synthetic exploration of this system, we encountered a new compound of relevance to the factors stabilizing the $TiAl_3$ structure. In our first such experiment, we annealed a Zr:Al:Sn mixture (1:2.8:2.3) using a temperature profile involving a short 24 h period at 900°C to promote melt formation and 2 weeks of annealing at 600°C. The powder X-ray diffraction pattern of the product is presented in Figure 7a, where peaks for $ZrSn_2$ and unreacted Sn are joined by indications of third phase whose peaks could not be matched to any known compound. EDS analysis of the sample confirmed the presence of $ZrSn_2$ (measured composition: $ZrSn_{1.95(6)}$), elemental Sn, and yielded the composition $ZrAl_{2.73(5)}Sn_{0.43(3)}$ for the third phase (see Supporting Information).

In examining the sample, well-faceted, dark gray crystals were picked from the surrounding Sn matrix. Their single crystal X-ray diffraction patterns revealed a body-centered tetragonal unit cell with $a \approx 3.99$ Å and $c \approx 9.09$ Å. After the collection of full data sets, inspection of the systematic absences suggested the space group $I4/mmm$. The resulting structure solution yielded three crystallographically distinct positions consistent with the $TiAl_3$ type, with one being assigned to Zr and the remaining two initially to Al. Refinement of this structure resulted in large Fourier difference peaks corresponding to additional electron density at one of these Al sites (4d). This site was thus modeled as partially occupied by Al and Sn with a total occupancy of 1.0. The refinement then led to a $TiAl_3$-type structure of composition $ZrAl_{2.605(6)}Sn_{0.395(6)}$ with $R(I>3\sigma) = 0.98$, and the largest residual electron density peak being less than 1 electron/Å^3. Details concerning this structure refinement are presented in the left-hand column of Table 1.

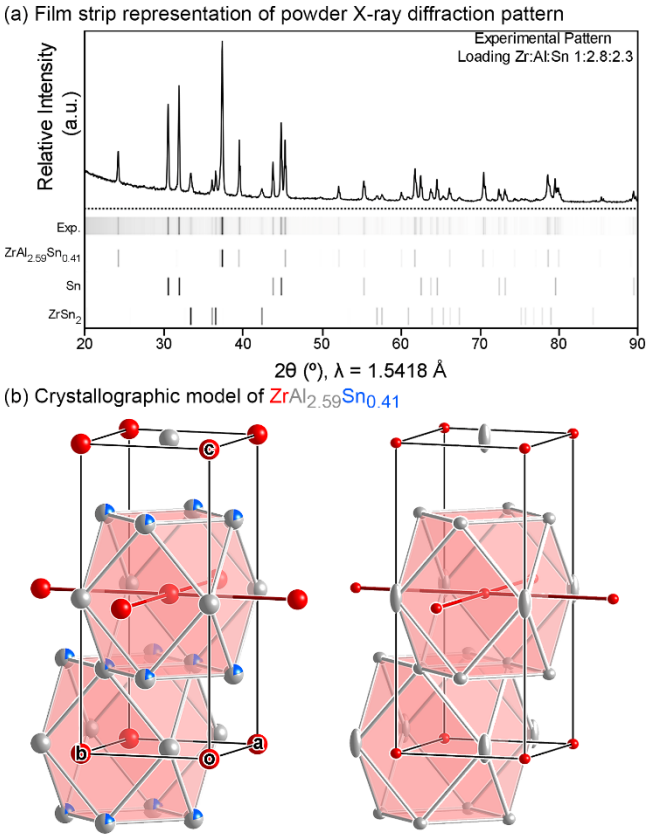

Figure 7. Experimental investigation of $ZrAl_{3-x}Sn_x$. (a) Powder X-ray diffraction pattern of the product from a sample with nomination composition Zr:Al:Sn = 1:2.8:2. The experimental pattern is shown above the dotted line as an intensity vs 2θ profile, while film strip representations of the experimental and simulated patterns are given below. (b) The crystal structure of $ZrAl_{3-x}Sn_x$ with x = 0.41 refined against single crystal X-ray diffraction data, show with a ball-and-stick representation (left) and with 75% probability ellipsoids (right).

After obtaining this new ternary Zr-Al-Sn compound, we set out to synthesize it in a more direct fashion. Samples were prepared with Zr:Al:Sn ratios ranging from near stoichiometric (1:3:0.5) to Sn rich (1:2:3) Each sample was characterized by powder X-ray diffraction and single crystal X-ray diffraction to assess the phase purity and crystal quality respectively. We noticed that better single crystal quality was obtained in Sn rich samples, suggesting that crystal growth is promoted within a Sn self-flux.[60] In the single crystal refinements from Sn-poor and Sn-rich samples, the Sn occupation on the mixed site differed by less than 1 at %, suggesting that the homogeneity range for this phase, if any, is extremely narrow (Table 1).

In contrast to the $ZrAl_3$-type structure of the unsubstituted $x = 0$ end member, $ZrAl_{3-x}Sn_x$ ($x \approx 0.4$) crystallizes in the $TiAl_3$ structure type. Here, the Zr atoms are each coordinated in a cuboctahedral fashion by Al/Sn atoms. As shown in Figure 7b, within the main group sublattice a clear site Al/Sn preference can be noted between the two symmetry-distinct sites, the one positioned in the Zr square nets perpendicular to c (the 2b site) or one lying between the Zr square nets (the 4d site). The former site is found to be exclusively occupied by Al, while the latter exhibits mixing between Al and Sn.

Table 1: Crystal Data for $ZrAl_{3-x}Sn_x$ Crystals from Samples with Different Sn Loadings

Loading (Zr: Al:Sn)	1:0.75:2.8	1:2.8:2.3
Refined Comp.	$ZrAl_{2..605(6)}Sn_{0.395}$	$ZrAl_{2.593(7)}Sn_{0.407}$
Crystal Color	Dark gray with metallic sheen	
Crystal Dim. (mm)	0.04×0.03×0.03	0.03×0.03×0.04
Radiation Source	Mo Kα (λ = 0.71073 Å)	
Collection Temp.	Room Temperature	
Pearson Symbol	*tI*8	
Space Group	*I*4/*mmm* (139)	
a (Å)	3.9909(9)	3.992(9)
c (Å)	9.0876(19)	9.091(2)
V (Å^3)	144.74(6)	144.10(7)
Abs. Coeff. (mm^{-1})	7.575	7.664
Θ_{min}, Θ_{max}	4.49, 44.85	4.48, 45.31
Number of Reflns.	9021	8042
$R_{int}(I>3\sigma$, all)	2.20/2.22	5.12/5.30
Unique reflns ($I>3\sigma$, all)	210, 208	182,210
Number of Params	9	9
$R(I>3\sigma)$, $R_w(I>3\sigma)$	0.73, 0.79	2.03, 2.46
R(all), R_w(all)	1.19, 1.20	2.28, 2.35
S ($I>3\sigma$, all)	0.98, 0.82	1.47, 1.41
$\Delta\rho_{max}$, $\Delta\rho_{min}$ (e$^-$/Å^3)	0.28, -0.28	1.02, -1.03

In the anisotropic thermal ellipsoids, there is one notable feature (Figure 7b, right). The probability ellipsoid for the Al atom at 2b site exhibits significant elongation along c, whereas those of the remaining sites are more spherical. Our CP schemes for the $TiAl_3$ type in Figures 5 and 6 offer an explanation of this anisotropy: the CP distribution around this site bear negative pressures directed along $\pm c$, and positive lobes in the perpendicular directions. Such quadrupolar CP distributions are associated with soft atomic motions, as can been seen in the lowest frequency optical modes at the Γ point in the Supporting Information. Another potential contributing factor is the Sn/Al mixed occupancy in the layers of 4d sites above and below, which could create more static displacements.[61]

3.6. Electronic Relief in $ZrAl_{3-x}Sn_x$. As we saw above, the synthesis and experimental characterization of $ZrAl_{3-x}Sn_x$ demonstrates that partial substitution of Al by Sn in $ZrAl_3$ leads to a transition to the $TiAl_3$ type. Let's examine how this structural change can be understood in terms of the atomic size and valence electron count, factors shaping the relative stabilities of these two types. We begin with the electronic considerations. According to the 18–*n* rule, the $ZrAl_3$ and $TiAl_3$ types are electronically optimized at 13 and 14 electrons per T atom respectively. For the $x = 0$ end member, the electron count is 13 electrons/T atom, making the observed $ZrAl_3$-type structure electron precise. However, as each Sn atom substituted into the phase brings one additional valence electron, we would expect that Sn incorporation would increasingly stabilize the $TiAl_3$ type, with $x = 1.00$ corresponding to the ideal 14 electrons/T atom.

To test this idea, we constructed an ordered model with composition $ZrAl_2Sn$, in which Sn is placed on half of the 4d sites (those observed experimentally to have the highest affinity for this element). An example of such a pattern is shown in Figure 8a.

The resulting DOS distribution exhibits a clear pseudogap just below -6 eV in the midst of a dense block of Zr d states between -10 and -4 eV. The E_F of the structure lies just above the DOS minimum of the pseudogap, corroborating the electronic precision of the structure predicted by the 18–*n* rule. If we compare this to the situation of $ZrAl_3$ in the $TiAl_3$ structure type (Figure 3), it is clear that Sn substitution can play the role of raising the E_F from the lower shoulder of the pseudogap to a more favorable position.

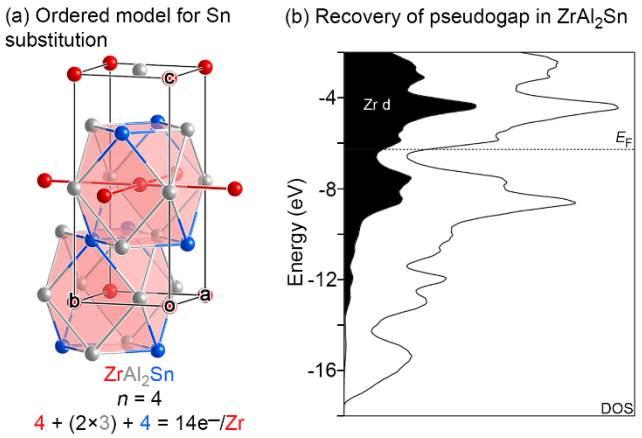

Figure 8. $TiAl_3$-type $ZrAl_2Sn$ as an 18–*n* structure. (a) An ordered model used in the electronic structure calculations, (b) The GGA-DFT DOS distribution calculated for this model. Compare the placement of the E_F here with that computed for $TiAl_3$-type $ZrAl_3$ in Figure 3.

Of course, $x = 1.0$ corresponds to a higher level of Sn substitution than is observed in $ZrAl_{3-x}Sn_x$, where $x \sim 0.4$. The close-correspondences between the DOS distributions of $TiAl_3$-type $ZrAl_3$ and $ZrAl_2Sn$, though, affirm that a simple rigid band model should be useful here. One can imagine lower Sn incorporation to simply lower the E_F relative to the DOS minimum. In this way, the valence electron count becomes intermediate between the ideal values for the two structure types, shifting the degree to which the $TiAl_3$ type is stabilized relative to the $ZrAl_3$ type.

3.7. Chemical Pressure and Electronegativity Guiding Sn Substitution. In our above analysis, we saw that Sn-substitution in $ZrAl_3$ stabilizes the $TiAl_3$ type $ZrAl_2Sn$ by increasing the valence electron count. This picture on its own, however, does not account for the distinct Al/Sn site preferences observed in $ZrAl_{3-x}Sn_x$ nor does it address the potential role that the larger metallic radius of Sn may play. In this final section, we will see how both factors contribute to the transition to the $TiAl_3$ type.

Elemental site preferences in intermetallics have long been investigated and can conceptually be interpreted by applying perturbation theory to an unsubstituted reference system. The major factors directing different elements to different sites are generally traced to differences in bonding strength (as through crystal orbital overlap or Hamilton population analysis) or to the differing electron populations on the sites (applying the notion of topological charge stabilization).[62-64] The DFT-CP method has also been recently applied in a complementary way, examining whether local pressures at a site could be soothed by substitution by a larger or smaller atom.[65,66] Here, we will consider how the atomic charges and CP scheme of an unsubstituted $TiAl_3$- and $ZrAl_3$-type T = Zr phase relate to the observed Sn substitution pattern in $ZrAl_{3-x}Sn_x$.

We will begin by examining again the CP scheme of $TiAl_3$-type $ZrAl_3$ (Figure 9a). This scheme is dominated by positive heteroatomic pressures between Zr and the in-plane Al atoms, which competes with the largest negative CPs in the Al sublattice. The presence of positive Zr-Al and negative Al-Al CPs on these in-plane Al sites (the Al 2b site) gives them a much more positive net atomic pressure than the Al atoms in the planes above and below along *c* (the Al4d site): +0.67 GPa vs. -9.41 GPa.

These differing pressures are suggestive of different affinities for substitution by Sn. The net positive atomic CP of the Al2b site shows the Al atom currently occupying the position is too large for its coordination environment. The placement of a larger Sn atom there would not be expected to be favorable. The negative pressure on the remaining site, however, tells of a better scenario for Sn incorporation: the Al atom here is smaller overall than is optimal for this site, and a larger atom would be welcome. From this, we would expect Sn to preferentially substitute in the Al4d site in the $TiAl_3$ type.

In Figure 9, we test these expectations with CP schemes calculated for three ordered models of $ZrAl_2Sn$: one with Sn placed in the 2b sites, the others with Sn occupying half of the 4d sites in patterns that are either staggered or unstaggered between adjacent layers. The placement into the 2b sites leads to the most intense Zr-Sn pressures. The unstaggered 4d configuration does not look much more favorable, with intense Zr-Sn pressures being counteracted by concentrated Sn-Al and Al-Al negative CPs. By contrast, the staggered 4d geometry has soothed CP features even relative to the unsubstituted compound $ZrAl_3$. This is also reflected in the energetics with the staggered geometry being more stable than the other configurations by more than 0.4 eV per atom. These results confirm the prediction that Sn should prefer the 4d site, but add the caveat that their staggered placement is important.

The atomic charges derived from a Bader analysis on the $TiAl_3$-type $ZrAl_3$ structure yields a similar story. The Bader charges on the Al2b and Al4d sites are respectively -0.185 and -0.212. As Sn is more electronegative than Al (Pauling electronegativities: 1.96 and 1.61), it would be predicted to prefer the site with the more negative charge. In this regard, the electronegativity factor concurs with the

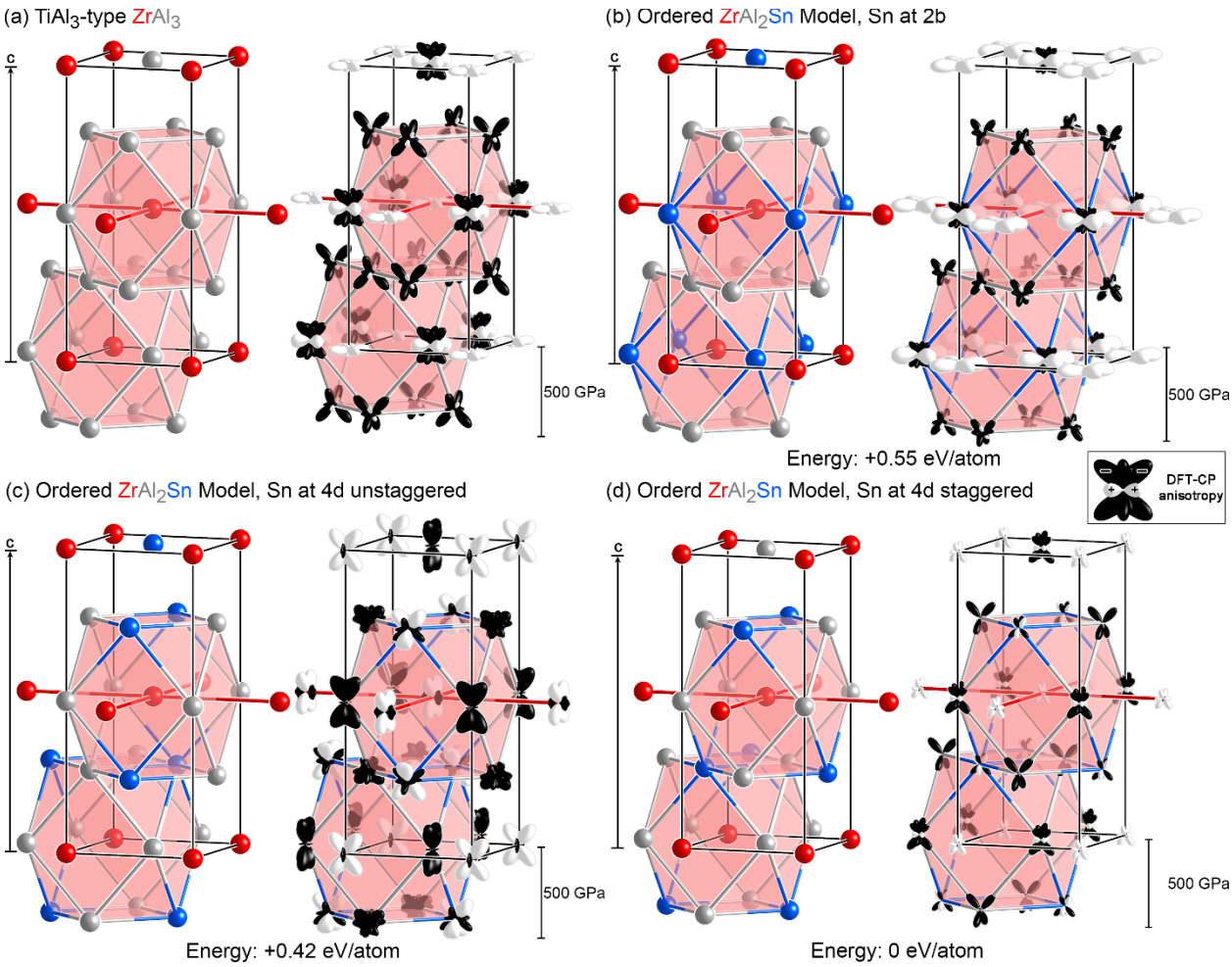

Figure 9. CP schemes and relative energies for ordered models of a $TiAl_3$-type $ZrAl_2Sn$ structure. (a) The CP scheme of $TiAl_3$-type $ZrAl_3$ for reference. (b) Full substitution with Sn at the 2b site. (c) Substitution with Sn at one half of the 4d positions with no staggering between ab-layers. (d) A second ordered model of Sn substitution at half of the 4d positions, this time in a staggered manner such that the I-centering of the lattice is maintained.

CP scheme in directing Sn toward the Al4d site, and these predictions match the observed preferences in the structure refinement.

These factors directing Sn to the 4d sites can also be connected to the stabilization of the $TiAl_3$ type over the $ZrAl_3$ one. The 4d sites of the $TiAl_3$ type make up the square nets of Al atoms defining the stacking shift layers that break up the T-T isolobal bonding framework relative to the $AuCu_3$ type. In the $ZrAl_3$ type, the frequency of these stacking shift layers is reduced by a factor of two, leading to only half the number of sites with a strong affinity for Sn. A composition near $ZrAl_2Sn$ would involve near-complete filling of the stacking shift layers with Sn. As these are the points where Al-Al repulsion destabilized the $ZrAl_3$ type with T = Ti, a high population of larger Sn atoms in these layers would likely create similar conflicts.

4. CONCLUSIONS

In this Article, we have investigated the factors leading $TiAl_3$ to break the 18–*n* rule by forming its own type, even as the $ZrAl_3$ type represents a plausible and electron-precise alternative. By combining total energies, CP schemes, DOS distributions, and energy partitions in raMO functions, we saw that the favorability of the electron-precise $ZrAl_3$-type structure vs. the $TiAl_3$-type is significantly reduced for T = Ti relative to T = Zr. This difference is traced to a simple packing issue: given the smaller size of the Ti atoms, the formation of the additional T-T bonds in the $ZrAl_3$ type would require unfavorable contacts between Al atoms elsewhere in the structure. The conflicts encountered here between preferred T-T connectivity and atomic size requirements highlight how frustration can arise even in systems nominally derived from a coloring of the simple FCC structure.

Following this theoretical exploration, we presented the synthesis, structure, and analysis of a compound that illustrates these factors at work, $ZrAl_{3-x}Sn_x$ ($x \sim 0.4$). The addition of Sn serves to promote a transition from the $ZrAl_3$ type structure of the $x = 0$ endmember to the $TiAl_3$ type by (1) raising the electron count and thus reducing the drive for five rather than four isolobal bonds on each Zr atom, and (2) increasing the packing costs to maintaining the fifth isolobal bond.

Both of these stories—the preference of $TiAl_3$ for its own type vs. the $ZrAl_3$ type, and the reverse transition upon incorporating Sn into $ZrAl_3$—provide illustrations of the Frustrated and Allowed Structural Transitions (FAST) principle[67-69] applied recently to the explanation of several incommensurately modulated structures. The FAST principle serves a guide to navigating situations where several factors, such as electronics and atomic packing factors

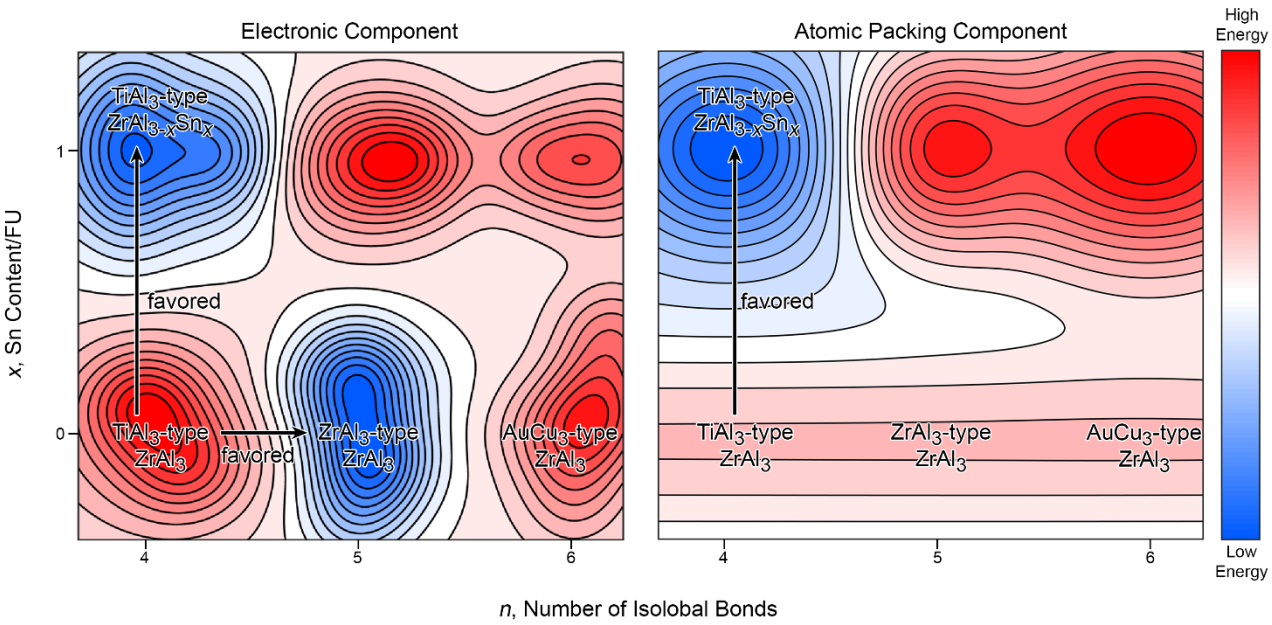

Figure 10. Schematic energy landscapes for $ZrAl_{3-x}Sn_x$ structures in terms of the number of isolobal bonds (n) and Sn atoms (x) per Zr atom.

commonly evoked in intermetallics, simultaneously influence the stabilities of two related structures. It states that a structural transformation (whether between two existing structures with changes in conditions, composition, etc. or from a hypothetical reference structure to a more stable one) is more likely to occur when those factors concur that the change is favorable (allowed transitions). In cases where there is disagreement about the favorability of a structural change, the conditions under which the transition occurs are expected to be very limited (frustrated transitions).

Within this framework, the formation of $ZrAl_3$-type $TiAl_3$ would be classified as frustrated since the electronic drive for five isolobal bonds around each T atom is resisted by the Al-Al repulsion it would create. With this conflict, it is not clear immediately which of the structure types is preferable, and indeed the energy difference between them for T = Ti is calculated to be extremely small.

By contrast, the transition to the $TiAl_3$ type by partially substituting Al with Sn into $ZrAl_3$ is allowed, as is shown schematically in Figure 10. Here, we plot a qualitative energy landscape for electronic and atomic packing components in the $ZrAl_{3-x}Sn_x$ system, and how the energies vary with changes in Sn content and the number of isolobal bonds. For $x = 0$, the $ZrAl_3$ structure type has few relatively little packing issues and adheres to the 18–n rule. It thus appears as a minimum in both maps. As x is increased, the higher electron count of the Sn and its preference for the more sterically congested shift layers leads the minimum to migrate to the $TiAl_3$ type. There is potential for a valley to occur between $(n, x) = (5, 0)$ and $(4, 1)$, which could indicate the possibility for incommensurate derivatives to form. Along these lines, an exciting avenue for future work is to determine if a similar balance of forces plays a role in the incommensurability exhibited by non-stoichiometric variants of $TiAl_3$.[70]

These results hint that while 18–n electron counts are quite frequently associated with pseudogaps in intermetallic chemistry, the details of how and whether this rule is adhered to may be tightly coordinated with atomic size effects. In this case, we saw that quite different interatomic pressures arise at Al-Al contacts, even at the same distance, depending on their level of involvement with isolobal T-T bonds. For the system with smaller T atoms, this created tension that largely negated the benefits of full realization of an 18–n bonding scheme. Similar situations could underlie other cases where the 18–n rule is broken.

Another intriguing possibility is that similar applications of the FAST principle could explain the conditions under which systems will place electrons in main-group-based bonding states distinct from the T atoms. For example, the 18.33 electrons/T atom count of Ir_3Sn_7 corresponds to a pseudogap with 17 of those electrons belonging to Ir atoms in dumbbells (n = 1), and the remaining 1.33 electrons/Ir atom populating Sn-Sn single bonds elsewhere in the structure.[40] In such cases, the overall electron count for the system is given by a more general 18–n+m scheme, in which m electrons are held by the main group atoms independently of the T atoms. Through the addition of the m parameter, the same electron count can lead to different T-T connectivities, with increases in m simply being compensated by increases in n. Atomic size effects of the type investigated here could determine which n, m configuration will be most favorable for a given combination of elements and composition. We are excited about exploring this possibility through the theoretical investigation of isoelectronic structures with different values of n and m.

ASSOCIATED CONTENT

Supporting Information. Additional crystallographic information; Energy Dispersive X-ray spectroscopy data; additional computational details; additional DOS distributions; CP schemes calculated with different free-ion densities corresponding to different percentages of the Bader charges comparison of CP features with selected phonon modes. Crystallographic Information Files (CIFs) have been deposited in the Inorganic Crystal Structure Database

(ICSD), and may be retrieved with the deposition numbers 2047862 and 2047952.

AUTHOR INFORMATION

Corresponding Author

*e-mail: danny@chem.wisc.edu

ACKNOWLEDGMENTS

We would like to thank Dr. Ilia Guzei and Amelia Wheaton of the UW-Madison Molecular Structures Laboratory for the data collection on the Bruker Quazar APEX2 diffractometer, whose purchase was made possible by the generous gift of Paul J. and Margaret M. Bender. We are also grateful to Dr. Hillary Mitchell Warden for discussion of the FAST principle and its development, and to Bil Schneider for his aid with the EDS sample preparation and instrument operation. We gratefully acknowledge the financial support of the National Science Foundation (NSF) through grant DMR-1809594. DCF expresses his appreciation to the Vilas Trust for a Vilas Associate Award. This work includes calculations that used the computing resources supported by the NSF Grant CHE-0840494.

REFERENCES

(1) Stirling, A. Assessing Hypervalency in Iodanes. *Chem Eur. J.* **2018**, *24*, 1709-1713.

(2) A. Papoian, G.; Hoffmann, R. Hypervalent Bonding in One, Two, and Three Dimensions: Extending the Zintl–Klemm Concept to Nonclassical Electron-Rich Networks. *Angew. Chem. Int. Ed.* **2000**, *39*, 2408-2448.

(3) Grabowski, S. J. Boron and other Triel Lewis Acid Centers: From Hypovalency to Hypervalency. *ChemPhysChem* **2014**, *15*, 2985-2993.

(4) Berns, V. M.; Fredrickson, D. C. Problem Solving with Pentagons: Tsai-Type Quasicrystal as a Structural Response to Chemical Pressure. *Inorg. Chem.* **2013**, *52*, 12875-12877.

(5) Steurer, W. Why are quasicrystals quasiperiodic? *Chem. Soc. Rev.* **2012**, *41*, 6719-6729.

(6) Shechtman, D.; Blech, I.; Gratias, D.; Cahn, J. W. Metallic Phase with Long-Range Orientational Order and No Translational Symmetry. *Phys. Rev. Lett.* **1984**, *53*, 1951.

(7) Tolman, C. The 16 and 18 electron rule in organometallic chemistry and homogeneous catalysis. *Chem. Soc. Rev.* **1972**, *1*, 337-353.

(8) Stiegman, A. E.; Tyler, D. R. Reactivity of Seventeen- and Nineteen-Valence Electron Complexes in Organometallic Chemistry. *Comments Inorg. Chem.* **1986**, *5*, 215-245.

(9) Eisenstein, O.; Hoffmann, R. Transition-metal complexed olefins: how their reactivity toward a nucleophile relates to their electronic structure. *J. Am. Chem. Soc.* **1981**, *103*, 4308-4320.

(10) Yannello, V. J.; Fredrickson, D. C. Generality of the 18-*n* Rule: Intermetallic Structural Chemistry Explained through Isolobal Analogies to Transition Metal Complexes. *Inorg. Chem.* **2015**, *54*, 11385-11398.

(11) Bergerhoff, G.; Hundt, R.; Sievers, R.; Brown, I. The Inorganic Crystal Structure Database. *J. Chem. Inf. Comput. Sci.* **1983**, *23*, 66-69.

(12) Dshemuchadse, J.; Steurer, W. Some statistics on intermetallic compounds. *Inorg. Chem.* **2015**, *54*, 1120-1128.

(13) Zalutskii, I.; Kripyakevich, P. RAl_3 Compounds in Rare Earth-Aluminum Systems and Their Crystal Structures. *Sov. Phys.-Cryst.* **1967**, 394-397.

(14) Colinet, C.; Pasturel, A. Phase stability and electronic structure in $ZrAl_3$ compound. *J. Alloys Compd.* **2001**, *319*, 154-161.

(15) Ma, Y.; Romming, C.; Lebech, B.; Gjonnes, J.; Tafto, J. Structure refinement of Al_3Zr using single-crystal X-ray diffraction, powder neutron diffraction and CBED. *Acta Crystallogr. Sect. B: Struct. Sci.* **1992**, *48*, 11-16.

(16) Hong, T.; Watson-Yang, T. J.; Freeman, A. J.; Oguchi, T.; Xu, J.-h. Crystal structure, phase stability, and electronic structure of Ti-Al intermetallics: $TiAl_3$. *Phys. Rev. B* **1990**, *41*, 12462-12467.

(17) Jahnátek, M.; Krajčí, M.; Hafner, J. Interatomic bonding, elastic properties, and ideal strength of transition metal aluminides: A case study for A_3 (Ti and V). *Phys. Rev. B* **2005**, *71*, 024101.

(18) Norby, R.; Christensen, A. N.; Pedersen, E. Preparation and Structure of Al_3Ti. *Acta Chem. Scand. Ser. A.* **1986**, *40*, 157.

(19) Boulechfar, R.; Ghemid, S.; Meradji, H.; Bouhafs, B. FP-LAPW investigation of structural, electronic, and thermodynamic properties of Al_3V and Al_3Ti compounds. *Physica B: Condens. Matter* **2010**, *405*, 4045-4050.

(20) Chong, Z.; Hoffmann, R. An Unusual Electron Count and Electron-Deficient Multi-Center Bonding in One Class of Intermetallics: The $BaAl_4$, $CaAl_2Zn_2$, $CeMg_2Si_2$ and FCC Al Structures. *Z. Naturforsch., B: Chem. Sci.* **1986**, *41*, 292-320.

(21) Lee, S. Structural Diversity in Solid State Chemistry:A Story of Squares and Triangles. *Annu. Rev. Phys. Chem.* **1996**, *47*, 397-419.

(22) Another explanation for this series has been derived from the MOs of Al clusters. See: Condron, C. L.; Miller, G. J.; Strand, J. D.; Bud'ko, S. L.; Canfield, P. C. A New Look at Bonding in Trialuminides: Reinvestigation of $TaAl_3$. *Inorg. Chem.* **2003,** *42,* 8371-8376.

(23) Fredrickson, D. C. Electronic Packing Frustration in Complex Intermetallic Structures: The Role of Chemical Pressure in Ca_2Ag_7. *J. Am. Chem. Soc.* **2011**, *133*, 10070-10073.

(24) Engelkemier, J.; Berns, V. M.; Fredrickson, D. C. First-Principles Elucidation of Atomic Size Effects Using DFT-Chemical Pressure Analysis: Origins of $Ca_{36}Sn_{23}$'s Long-Period Superstructure. *J. Chem.* **2013**, *9*, 3170-3180.

(25) Engelkemier, J.; Fredrickson, D. C. Chemical Pressure Schemes for the Prediction of Soft Phonon Modes: A Chemist's Guide to the Vibrations of Solid State Materials. *Chem. Mater.* **2016**, *28*, 3171-3183.

(26) Hilleke, K. P.; Fredrickson, D. C. Discerning Chemical Pressure amidst Weak Potentials: Vibrational Modes and Dumbbell/Atom Substitution in Intermetallic Aluminides. *J. Phys. Chem. A* **2018**, *122*, 8412-8426.

(27) Kresse, G.; Furthmüller, J. Efficient iterative schemes for ab initio total-energy calculations using a plane-wave basis set. *Phys. Rev. B* **1996**, *54*, 11169-11186.

(28) Kresse, G.; Furthmüller, J. Efficiency of ab-initio total energy calculations for metals and semiconductors using a plane-wave basis set. *Comput. Mater. Sci.* **1996**, *6*, 15-50.

(29) Kresse, G.; Hafner, J. Ab initio molecular-dynamics simulation of the liquid-metal–amorphous-semiconductor transition in germanium. *Phys. Rev. B* **1994**, *49*, 14251.

(30) Kresse, G.; Hafner, J. Ab initio molecular dynamics for liquid metals. *Phys. Rev. B* **1993**, *47*, 558.

(31) Perdew, J. P.; Chevary, J.; Vosko, S.; Jackson, K. A.; Pederson, M. R.; Singh, D.; Fiolhais, C. Erratum: Atoms, molecules, solids, and surfaces: Applications of the generalized gradient approximation for exchange and correlation. *Phys. Rev. B* **1993**, *48*, 4978.

(32) Perdew, J. P.; Chevary, J. A.; Vosko, S. H.; Jackson, K. A.; Pederson, M. R.; Singh, D. J.; Fiolhais, C. Atoms, molecules, solids, and surfaces: Applications of the generalized gradient approximation for exchange and correlation. *Phys. Rev. B* **1992**, *46*, 6671-6687.

(33) Blöchl, P. E. Projector augmented-wave method. *Phys. Rev. B* **1994**, *50*, 17953-17979.

(34) Landrum, G.; Glassey, W. Yet Another Extended Hückel Molecular Orbital Package (YAeHMOP) Version 3.0 User Manual. **2006**.

(35) Bader, R. F. Atoms in molecules. *Acc. Chem. Res.* **1985**, *18*, 9-15.

(36) Henkelman, G.; Arnaldsson, A.; Jónsson, H. A fast and robust algorithm for Bader decomposition of charge density. *Comput. Mater. Sci.* **2006**, *36*, 354-360.

(37) Sanville, E.; Kenny, S. D.; Smith, R.; Henkelman, G. Improved grid-based algorithm for Bader charge allocation. *J. Comput. Chem.* **2007**, *28*, 899-908.

(38) Tang, W.; Sanville, E.; Henkelman, G. A grid-based Bader analysis algorithm without lattice bias. *J. Phys.: Condens. Matter* **2009**, *21*.

(39) Yannello, V. J.; Fredrickson, D. C. Orbital Origins of Helices and Magic Electron Counts in the Nowotny Chimney Ladders: the 18-n Rule and a Path to Incommensurability. *Inorg. Chem.* **2014**, *53*, 10627-10631.

(40) Yannello, V. J.; Kilduff, B. J.; Fredrickson, D. C. Isolobal Analogies in Intermetallics: The Reversed Approximation MO Approach and Applications to $CrGa_4$- and Ir_3Ge_7-Type Phases. *Inorg. Chem.* **2014**, *53*, 2730-2741.

(41) Stacey, T. E.; Fredrickson, D. C. Perceiving Molecular Themes in the Structures and Bonding of Intermetallic Phases: The Role of Hückel Theory in an *ab initio* Era. *Dalton Trans.* **2012**, *41*, 7801-7813.

(42) Gonze, X. A brief introduction to the ABINIT software package. *Z. Kristallogr.* **2005**, *220*.

(43) Gonze, X.; Amadon, B.; Anglade, P.-M.; Beuken, J.-M.; Bottin, F.; Boulanger, P.; Bruneval, F.; Caliste, D.; Caracas, R.; Côté, M. ABINIT: First-principles approach to material and nanosystem properties. *Comput. Phys. Comm.* **2009**, *180*, 2582-2615.

(44) Gonze, X.; Jollet, F.; Abreu Araujo, F.; Adams, D.; Amadon, B.; Applencourt, T.; Audouze, C.; Beuken, J. M.; Bieder, J.; Bokhanchuk, A.; Bousquet, E.; Bruneval, F.; Caliste, D.; Côté, M.; Dahm, F.; Da Pieve, F.; Delaveau, M.; Di Gennaro, M.; Dorado, B.; Espejo, C.; Geneste, G.; Genovese, L.; Gerossier, A.; Giantomassi, M.; Gillet, Y.; Hamann, D. R.; He, L.; Jomard, G.; Laflamme Janssen, J.; Le Roux, S.; Levitt, A.; Lherbier, A.; Liu, F.; Lukačević, I.; Martin, A.; Martins, C.; Oliveira, M. J. T.; Poncé, S.; Pouillon, Y.; Rangel, T.; Rignanese, G. M.; Romero, A. H.; Rousseau, B.; Rubel, O.; Shukri, A. A.; Stankovski, M.; Torrent, M.; Van Setten, M. J.; Van Troeye, B.; Verstraete, M. J.; Waroquiers, D.; Wiktor, J.; Xu, B.; Zhou, A.; Zwanziger, J. W. Recent developments in the ABINIT software package. *Comput. Phys. Comm.* **2016**, *205*, 106-131.

(45) Gonze, X.; Beuken, J. M.; Caracas, R.; Detraux, F.; Fuchs, M.; Rignanese, G. M.; Sindic, L.; Verstraete, M.; Zerah, G.; Jollet, F.; Torrent, M.; Roy, A.; Mikami, M.; Ghosez, P.; Raty, J. Y.; Allan, D. C. First-principles computation of material properties: the ABINIT software project. *Comput. Mater. Sci.* **2002**, *25*, 478-492.

(46) Hartwigsen, C.; Gœdecker, S.; Hutter, J. Relativistic separable dual-space Gaussian pseudopotentials from H to Rn. *Phys. Rev. B* **1998**, *58*, 3641.

(47) Oliveira, M. J.; Nogueira, F. Generating relativistic pseudo-potentials with explicit incorporation of semi-core states using APE, the Atomic Pseudo-potentials Engine. *Comput. Phys. Commun.* **2008**, *178*, 524-534.

(48) Brandenburg, K.; Putz, H. In *Program for Phase Identification from Powder Diffraction "Match!" ver. 3.7. 1.132*; Crystal Impact: Bonn, Germany, 2019.

(49) Agilent Technologies Ltd: Yarnton, Oxfordshire, England, 2014.

(50) Bruker-AXS; Version 8.30C ed. Madison, Wisconsin, USA, 2013.

(51) Bruker-AXS; Version 2017.3.0 ed. Madison, Wisconsin, USA, 2017.

(52) Krause, L.; Herbst-Irmer, R.; Sheldrick, G. M.; Stalke, D. Comparison of silver and molybdenum microfocus X-ray sources for single-crystal structure determination. *J. Appl. Crystallogr.* **2015**, *48*, 3-10.

(53) Oszlányi, G.; Sütő, A. Ab initio structure solution by charge flipping. *Acta Crystallogr. Sect. A: Found. Crystallogr.* **2004**, *60*, 134-141.

(54) Palatinus, L.; Chapuis, G. SUPERFLIP–a computer program for the solution of crystal structures by charge flipping in arbitrary dimensions. *J. Appl. Crystallogr.* **2007**, *40*, 786-790.

(55) Petříček, V.; Dušek, M.; Palatinus, L. Crystallographic computing system JANA2006: general features. *Z. Kristallogr. Cryst, Mater.* **2014**, *229*, 345-352.

(56) *International Tables for Crystallography Vol. A: Space Group Symmetry*; Hahn, Th., Ed. International Union of Christallography: Chester, England, 2004.

(57) Braun, J.; Ellner, M. Phase equilibria investigations on the aluminum-rich part of the binary system Ti-Al. *Metall. Mat. Trans. A* **2001**, *32*, 1037-1047.

(58) Greenwood, N. N.; Earnshaw, A. In *Chemistry of the Elements (Second Edition)*; Butterworth-Heinemann: Oxford, 1997, p 216-267.

(59) Bochvar, N. R.; Sheftel, E. N. Aluminum-Tin-Zirconium. *Ternary Alloys* **1993**, *8*, 389-397.

(60) Canfield, P. C.; Fisk, Z. Growth of single crystals from metallic fluxes. *Philos. Mag. B* **1992**, *65*, 1117-1123.

(61) We also created a structural model in which the Al atom at the 2b site is replaced with a split site, which 50% occupied Al atoms were placed at just above and below the 2*b* position (with their thermal parameters treated isotropically to avoid correlations with the z parameter). The refined structure has similar R-factors, goodness of fit parameters, and maximum peaks and holes in the Fourier difference map to those of the model presented in Table 1. However, this split site model has the disadvantage that it implies a static disorder between just two possible positions, which is not compatible with the numeous potential Sn/Al occupation patterns in the 2*b* coordination environment.

(62) Steinberg, S.; Dronskowski, R. The Crystal Orbital Hamilton Population (COHP) Method as a Tool to Visualize and Analyze Chemical Bonding in Intermetallic Compounds. *Crystals* **2018**, *8*, 225.

(63) Gimarc, B. M. Topological charge stabilization. *J. Am. Chem. Soc.* **1983**, *105*, 1979-1984.

(64) Miller, G. J. The "Coloring Problem" in Solids: How It Affects Structure, Composition and Properties. *Eur. J. Inorg. Chem.* **1998**, *1998*, 523-536.

(65) Hilleke, K. P.; Fredrickson, R. T.; Vinokur, A. I.; Fredrickson, D. C. Substitution Patterns Understood through Chemical Pressure Analysis: Atom/Dumbbell and Ru/Co Ordering in Derivatives of YCo_5. *Cryst. Growth Des.* **2017**, *17*, 1610-1619.

(66) Peterson, G. G. C.; Geisler, E. E.; Fredrickson, D. C. Intermetallic Reactivity: $Ca_3Cu_{7.8}Al_{26.2}$ and the Role of Electronegativity in the Stabilization of Modular Structures. *Inorg. Chem.* **2020**, *59*, 5018-5029.

(67) Folkers, L. C.; Mitchell Warden, H. E.; Fredrickson, D. C.; Lidin, S. Entropy-Driven Incommensurability: Chemical Pressure-Guided Polymorphism in PdBi and the Origins of Lock-In Phenomena in Modulated Systems. *Inorg. Chem.* **2020**, *59*, 4936-4949.

(68) Mitchell Warden, H. E.; Lee, S. B.; Fredrickson, D. C. Frustrated and Allowed Structural Transitions at the Limits of the $BaAl_4$ Type: The

(3 + 2)D Modulated Structure of $Dy(Cu_{0.18}Ga_{0.82})_{3.71}$. *Inorg. Chem.* **2020**, *59*, 10208-10222.

(69) Mitchell Warden, H. E.; Voyles, P. M.; Fredrickson, D. C. Paths to Stabilizing Electronically Aberrant Compounds: A Defect-Stabilized Polymorph and Constrained Atomic Motion in $PtGa_2$. *Inorg. Chem.* **2018**, *57*, 13880-13894.

(70) Loiseau, A.; Van Tendeloo, G.; Portier, R.; Ducastelle, F. Long period structures in $Ti_{1+x}Al_{3-x}$ alloys : experimental evidence of a devil's staircase? *J. Phys. France* **1985**, *46*, 595-613.

For Tables of Contents Use Only

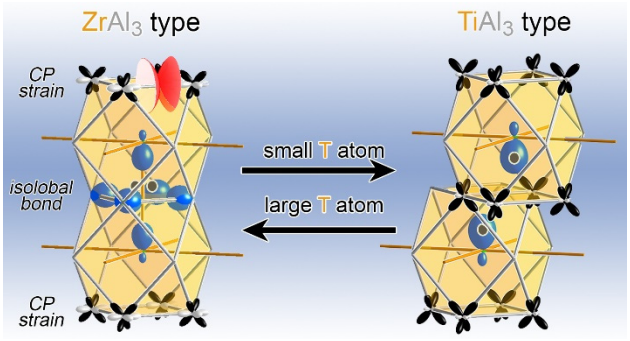

Synposis: We investigate the factors leading $TiAl_3$, to break the 18-*n* rule. DFT-Chemical Pressure analysis reveals a tension in $TiAl_3$ between the formation of the necessary T-T isolobal bonds and the space requirements of Al-Al contacts not supporting these interactions. This picture elucidates the transition of $ZrAl_3$ to the $TiAl_3$-type upon partial Sn substitution to form the new phase $ZrAl_{2.6}Sn_{0.4}$, and may be generalizable to violations of the 18–*n* rule in other systems.